Linear trends in cloud top height from passive observations in the oxygen A-band

L. Lelli[1], A. A. Kokhanovsky[*,1], V. V. Rozanov[1], M. Vountas[1], and J. P. Burrows[1]

[1]Institute of Environmental Physics and Remote Sensing, University of Bremen, Otto-Hahn-Allee 1, 28334 Bremen, Germany
[*]now at EUMETSAT, Eumetsat Allee 1, D-64295 Darmstadt, Germany

Correspondence to: L. Lelli (luca@iup.physik.uni-bremen.de)

Abstract. Measurements by the hyperspectral spectrometers GOME, SCIAMACHY, and GOME-2 are used to determine the rate of linear change (and trends) in cloud top height (CTH) in the period between June 1996 and May 2012. The retrievals are obtained from Top-Of-Atmosphere (TOA) backscattered solar light in the oxygen A-band using the Semi-Analytical CloUd Retrieval Algorithm SACURA. The physical framework relies on the asymptotic equations of radiative transfer, valid for optically thick clouds. Using linear least-squares techniques, a global trend of -1.78 ± 2.14 m yr^{-1} in deseasonalised CTH has been found, in the latitude belt within $\pm 60°$, with diverging tendencies over land ($+0.27 \pm 3.2$ m yr^{-1}) and ocean (-2.51 ± 2.8 m yr^{-1}). The El Niño-Southern Oscillation (ENSO), strongly coupled to CTH, forces clouds to lower altitudes. The global ENSO-corrected trend in CTH amounts to -0.49 ± 2.22 m yr^{-1}. At a global scale, no explicit regional pattern of statistically significant trends (at 95% confidence level, estimated with bootstrap technique) have been found, which would be representative of typical natural synoptical features. One exception is North Africa, which exhibits the strongest upward trend in CTH sustained by an increasing trend in water vapor.

1 Introduction

Tropospheric clouds are main players in the Earth's climate system. Characterization of long-term global cloud properties (top and bottom height, optical thickness and albedo, effective radius of droplets) aims to support radiation budget assessments as well as trace gas retrievals, and analysis of cloud interactions with aerosol particles and gases in the atmosphere. The altitude of a cloud plays a cardinal role because clouds at different heights (i.e., temperatures) exert different feedbacks. High-altitude clouds absorb infrared radiation that comes from the lower atmosphere and radiate like

1

blackbodies. Since the temperature contrast between elevated clouds and lower atmosphere is high, the clouds have a positive contribution on the local net energy balance. At the same time, their albedo is small because they are, in most cases, comparably thin. Thus, they can warm the atmosphere more than they cool it, exerting a positive feedback.

Conversely, low-altitude clouds are strongly reflecting objects owing to their high optical density but they ineffectually shield infrared radiation emitted by atmospheric gases to the outer space. The reason is that the temperature of low clouds is closer to the temperature of the ground and the local net energy balance is close to zero. These clouds in turn can cool the climate system more than they warm it and thus exert a negative feedback.

Loeb et al. (2012) observed this mechanism in a study that focused on clouds in the tropical belt. However, this situation may change when considering the Pacific Northeast over a decadal time window. Evidence of a positive feedback by low-level clouds has already been demonstrated (Clement et al., 2009). It is therefore likely that no general description is possible on a global scale and regional studies should be conducted instead.

Moreover, a critical aspect of any trend analysis is that, due to the limitation of a relatively short derived CTH time serie, no statistical significance may be found. Previous works do not provide clear indications. The analysis of the 7-year GOME record (June 1996 – May 2003) by Loyola et al. (2010) shows a change of $-4.8 \, \mathrm{m \, yr^{-1}}$ for the latitudinal belt within $\pm 60°$. Davies and Molloy (2012) reported a decreasing global trend of $-40 \, \mathrm{m \, decade^{-1}}$, as seen by MISR on the Terra platform. Evan and Norris (2012) showed that the previous results were affected by instrumental artifacts. Corrected MISR time series exhibit opposite tendency, that is an increase of $+54 \, \mathrm{m \, decade^{-1}}$, supported by a MODIS (on Terra) upward trend of $+60.9 \, \mathrm{m \, decade^{-1}}$. The considered record length amounts to 8 years, from March 2003 throughout February 2010.

In the present study it has been attempted to extend the cloud records including measurements of the three sensors GOME, SCIAMACHY and GOME-2 (hereinafter termed GSG). Since the launch of GOME, back in 1995, more than 17 years of data are now available and they form the observational basis of the present analysis (June 1996 – May 2012).

The manuscript has the following structure. Section 2 describes how the monthly-sampled cloud record is calculated from measured radiances. Section 3 introduces the model used to derive the rate of linear change in cloud top height. Section 4 is devoted to the main results of the work. First, an analysis of ENSO as reflected in cloud properties is presented and trends in cloud top height are assessed. In the last section, the findings are summarized also giving conclusions and outlook for future work.

2

2 Data and Methods

The spaceborne nadir-viewing spectrometers Global Ozone Monitoring Experiment (GOME, Burrows et al. (1999)), Scanning Imaging Absorption spectrometer for Atmospheric CHartographY (SCIAMACHY, Bovensmann et al. (1999)) and GOME-2 (Callies et al., 2000) measure solar backscattered light at a spectral resolution of 0.24–1.48 nm (see Table 1 for their characteristics). At the time of processing, GOME L1b data were in their version 4.00 and SCIAMACHY L1b version 7.03 with consolidation degree U. GOME-2 L1b data for time window 01/2007–12/2009 were in reprocessed stage, while near-real time data have been used for 01/2010–05/2012. Cloud fraction is obtained from broadband Polarization Measuring Devices (PMD) measurements with the Optical Cloud Recognition Algorithm (OCRA) (Loyola and Ruppert, 1998). For GOME, cloud fraction is delivered in bundle with L1b data, while cloud fraction for GOME-2 is taken from the off-line L2 reprocessed dataset made available by DLR in the framework of EUMETSAT's O3M Satellite Application Facility. Cloud fraction for SCIAMACHY has been calculated at University of Bremen with the in-house OCRA implementation.

In particular, the sensors cover the wavelength range 758–772 nm (at ≈ 0.4 nm resolution) where is situated one of the absorption bands of molecular oxygen, the O_2 A-band. The A-band is exploited by the Semi-Analytical CloUd Retrieval Algorithm (SACURA) (Rozanov and Kokhanovsky, 2004) to generate cloud top height (CTH) records in the following way: given the local fractional cloud cover (f), the sun-normalised Earthshine reflectances are weighted with the Independent Pixel Approximation (IPA) (Marshak et al., 1995). In this way, the measured scene reflectance R_{mes} is scaled to the cloud reflectance R_{cl} generated by a full cloudy ($f = 1$) and a cloud-free ($f = 0$) pixel with

$$R_{mes} = f R_{cl} + (1-f) R_s. \tag{1}$$

The clear-sky reflectance R_s is substituted by the Minimum Lambert-Equivalent Reflectivity (MLER) taken from the global database Tropospheric Emission Monitoring Internet Service (TEMIS) (Koelemeijer et al., 2003).

It has been demonstrated (Kokhanovsky et al., 2007; Lelli et al., 2012) that cloud top height is not substantially affected by the scaling of the cloud reflection function with different values of fractional cloud cover as long as f is known from an independent source. This statement is true regardless of cloud fraction and of instrumental spatial resolution, because the algorithm makes use of spectral ratios. From a physical point of view, it is also clear that, on the coarse footprint scales of the sensors used in this work, the cloud reflectance is dominated by the contribution of photons scattered directly back to the platform and not by horizontal photon transport. This is not true for spatially better resolved instruments for which a cloud volume may have side lengths comparable with the footprint size.

The cloud optical thickness (COT) is retrieved in the continuum at 758 nm and used for the computation of the forward TOA cloud reflectance with asymptotic approximations of radiative

3

transfer (Kokhanovsky and Rozanov, 2004). Then, the minimal difference between R_{cl} and the forward spectrum (modeled with the analytical equations of radiative transfer) is iteratively looked for along the whole O_2 A-band, at the nominal spectral sampling of the instruments. The distinctive feature of SACURA is the modeling of clouds as scattering layers instead of Lambertian reflectors (Koelemeijer et al., 2001), therefore radiative transfer throughout, above and below the clouds is taken into account. A comprehensive description of the algorithm can be found in Lelli et al. (2012, and references therein), where also accuracy, validation and selection criteria of CTH retrievals are given.

Cloud top height retrievals (b) are firstly binned in 13 height layers (k) (see Table 2 for the grid definition), projected onto a equidistant rectangular grid of 0.5°sided-cells at latitude (i) and longitude (j), counted-averaged over all altitudes (being c_k the retrieval counts at height bin k) at month t and the CTH means h_t are computed with

$$h_t(i,j) = \frac{\sum_k c_{kt}(i,j)\, b_{kt}(i,j)}{\sum_k c_{kt}(i,j)}. \tag{2}$$

This formulation has been chosen for consistency with Evan and Norris (2012, Eq. 1). The values for h_t are plotted in Fig. 1 for global (top) and tropical (bottom plot) region. In both cases, the time series of the individual instruments exhibit in-phase seasonality for the respective overlapping months, whereas the relative offsets (top plot) cannot be explained by the mere diurnal cycle clouds have, owing to the different overpass time of the instruments which fly 1/2 hour ahead of each other, GOME-2 crossing first the equator at 9:30 AM. In case of multi-layered cloud systems it is expected that sensors with coarser footprints, such as GOME (320×40 km^2), will observe more high clouds at the expenses of low clouds as compared to finer resolved sensors, such as SCIAMACHY (60×40 km^2) and GOME-2 (80×60 km^2). On a individual pixel scale, this effect can be seen in Lelli et al. (2012, Fig. 8, p. 1559), in which a GOME-derived CTH was co-located with a ground-based radar-derived CTH for a three-layer cloudy scene. GOME retrieved the height of the uppermost cloud layer. On larger time and spatial scales, this situation is depicted in Fig. 2, which shows retrieval counts c_k (normalised to the total number of counts) as function of height bin k, for different instruments and for global (left) and tropical (mid plot) region. The right plot of Fig. 2 shows the count difference between GOME and SCIAMACHY in both global and tropical region. Especially in the tropics, where heterogeneity is frequent, GOME counts increase toward higher layers of the troposphere. These values can be devised as correction factors for the harmonisation of time series among the instruments, given that the same scene is sensed and no time lag occurs between different measurements. Therefore, in the current analysis, it is preferred to compute the CTH anomalies of Fig. 3 subtracting the climatological seasonal cycle for each instrument separately, in order to avoid the introduction of *post-hoc* artifacts in the record.

While the CTH anomalies from GOME and SCIAMACHY are in almost perfect agreement, the transition between SCIAMACHY and GOME-2 records is not smooth. The reason for discrepancies may be manifold. On one hand, a change in the PMD pixel definitions of GOME-2 was devised in

4

April 2008 (EUMETSAT, 2010), which may have impacted cloud fraction f and the cloud reflection function R_{cl} of Eq. 1. On the other hand, radiometric calibration issues may also influence retrievals

130 inferred from different instruments. For instance, van Diedenhoven et al. (2005) have shown that a difference of 20 hPa in surface pressure retrieved in the oxygen A-band by GOME and SCIA-MACHY could be corrected adding an offset of 0.86% to the TOA reflectance in the continuum at 756 nm. However, tests have shown (see Appendix A) that radiometric uncertainties have almost no impact in the retrieved CTH with SACURA. This is a feature of the algorithm, which is based on

135 spectral ratios and on the concurrent fit of CTH and CBH along the whole band.

For the ensuing analysis, the time series of GOME and SCIAMACHY have been joined in June 2003 because the on-board tape recorder of GOME broke down and global coverage wasn't provided after May 2003. Time series of SCIAMACHY and GOME-2 have been joined in May 2008. Given that SCIAMACHY is a thoroughly tested instrument and GOME-2 PMD definitions were updated

140 in April 2008, we used SCIAMACHY anomalies prior May 2008, even though GOME-2 data were available. For the rest of the time serie, GOME-2 anomalies were used, as both instruments converge and exhibit good overlap. In fact, both instruments sense the strong negative CTH anomaly in year 2011. This feature dominates the whole time serie and it gives us reasonable confidence that the order of magnitude as well as the sign of the CTH trend aren't substantially affected, when using

145 SCIAMACHY data.

3   Trend model

The basic requirement for the application of linear least-square regression is that the variable of interest is not persistent (Wilks, 2011). Persistence is the tendency for a variable to remain similar in time and is measured as the degree of temporal autocorrelation r_p. The dataset of this study is

150 sampled on a monthly basis, thus autocorrelation at lag p=1 reveals the degree of persistence that CTH has after one month. The left plot of Fig. 4 shows the autocorrelation r_p of CTH anomalies up to 4 months lag, for global and tropical region. It can be seen that in both cases the altitude of clouds does not exhibit almost any persistence. That is, the actual anomaly is not affected by values leading by one month. Since characteristic time scales of clouds range from minutes for individual

155 shallow cloud cumulus to many hours for large stratiform cloud systems, over a month their features are randomised by intervening winds and persistence is not found. Therefore methods for normally distributed (gaussian) variables can be applied, given that the dataset has been deseasonalised. In the right plot of Fig. 4 the mapped CTH autocorrelation signal (not exceeding r_p=0.13 over the Pacific Ocean) resembles ENSO-related patterns, stretching across the globe over the Atlantic and the Indian

160 Oceans.

The trend magnitude β is calculated, at latitude and longitude (i, j), with

$$Y_t(i,j) = \alpha(i,j) + \beta(i,j) \cdot X_t + \epsilon_t(i,j) \qquad t = 1, \ldots, 192 \tag{3}$$

5

where Y_t are the CTH anomalies, X is the temporal variable sampled at monthly step t, α and ϵ_t the offset and the random noise, respectively. We emphasize that the time series of absolute values have been neither corrected for the impact of spatial resolution nor fitted directly. This is because the time series of Fig. 1 are shifted and the three instruments have different sensing local times. The chosen strategy has been to regress time series of anomalies, instead. This approach is analogous to the customary technique described in Mieruch et al. (2008, Eq. 1, p. 495, and references therein) and is reported below for convenience.

Being Y_t the monthly mean of the variable of interest at time t (for each geolocation point on the map), μC_t the offsets of the regression line, S_t the seasonal component, ω the desired change rate of the variable at time step X_t and N_t the noise, in the r.h.s. of the following equation

$$Y_t = \mu C_t + S_t + \omega X_t + \delta U_t + N_t \tag{4}$$

the term δU_t describes the level shift δ allowed when concatenating time series from different instruments at time T_0, with a step function U_t defined as

$$U_t = \begin{cases} 0, \, t < T_0 \\ 1, \, t \geqslant T_0 \end{cases} \tag{5}$$

The removal of the sample mean for each respective month from the time serie of absolute values allows the seasonality to be accounted for. The term δU_t is incorporated by performing this step separately for each instrument. This is because the sample mean of anomalies is, by definition, centered about zero (Wilks, 2011) and the constant μ can be neglected (being μ the mean value of Y_t at time t=0). Eventually, Eq. 4 reduces to Eq. 3 and potential autocorrelative effects are embedded in the noise term.

Among the techniques for the estimation of confidence intervals of the trend magnitude β, the *bootstrap resampling* (Efron and Tibshirani, 1993) enables the treatment of potentially non-normal data without any assumption on the underlying probability distribution. It belongs to the group of nonparametric methods and the knowledge of the analytical form of the statistics is not required (Mudelsee, 2010). The guiding idea is the "plug-in" principle: a new scrambled dataset is drawn (resampling with replacement) from the original dataset and a new β' is calculated with Eq. 3. This procedure is repeated n times and an empirical sample distribution for β is estimated. This empirical distribution can be regarded as the approximated estimate to the unknown β distribution and σ_β can be associated with the random effects reflected in the data. The required confidence level is customary chosen as 95%, implying a 2.5% cutting-off probability level on either sides for a two-tailed distribution. When the probability density function of the unknown distribution is related to its standardised Gaussian approximation, the cutting-off level amounts to the mean value ≈ 1.96 standard deviations σ_β (Wilks, 2011, p.140). Therefore, at locations (i,j) where the ratio $|\beta/\sigma_\beta| > 2$, the trend magnitude β exceeds natural variability and is considered statistically significant.

6

Fig. 5 shows the normalised probability density function (PDF) and the cumulative density function (CDF) of β, calculated with 10^4 bootstrap resamples, for global (left), tropical (mid) regions and the Central East Pacific (right). The red tails of the PDF portray the confidence level calculated with the percentile method at 2.5% and 97.5% quantile and provide the estimate of the uncertainty associated with the trend value β. We note that the condition of normality is reasonably satisfied even in the region of highest autocorrelation (i.e., Central East Pacific, 170° W-120° W, 5° N-5° S), as can be seen in the right plot of Fig. 5. Moreover, Fig. 6 displays the theoretical residual quantiles, estimated after regression with the linear model and application of the parameter estimates $\hat{\alpha}$ and $\hat{\beta}$ of Eq. 3 against the sample distribution of global CTH anomalies. Since the majority of points cluster about the straight line, the linear model seems to be a reasonable assumption, given that the autocorrelation functions of Fig. 4 drops almost to zero after one month.

Therefore, the major process that still can influence the time serie is the quasi-stationary ENSO. Laken et al. (2012) indirectly came to similar conclusions, while analysing the effect of solar activity on cloud altitudes with MODIS Terra and Aqua measurements. Norris (2005) comes to the same conclusion as well. The ENSO periodicity is still matter of on-going research (Solomon and Newman, 2012) and it is not the focus of this work.

4 Results

4.1 Cloud property changes coupling to ENSO

The El-Niño-Southern Oscillation (ENSO) has been recognized as the largest natural fluctuation that can establish teleconnections and modulate cloud properties. ENSO has to be understood as the tie between two different processes (Trenberth, 1997): the term *El Niño* is assigned to a yearly warming of the ocean current which streams along the coasts of Peru and Ecuador in late December. Regularly, but not every year, a more pronounced warming of the wide tropical-east pacific pool occurs, driven by the magnitude of trade wind flows. The atmospheric component of this perturbation is termed *Southern Oscillation*. The opposite phase, namely *La Niña*, corresponds to a cooling of the pacific basin. Quantitatively, ENSO is identified when SST gradient changes over the Central East Pacific (170° W - 120° W, 5° N - 5° S) exceed ± 0.5° C, resulting in the standard Niño 3.4 climate index (U. S. National Centers for Environmental Prediction (NCEP), 1993).

In Fig. 7 the Niño 3.4 index has been plotted together with the unsmoothed CTH and CF anomalies for the 17 years of the GSG dataset and high (R = +0.77) and moderate (R = +0.31) correlations are observed for CTH and CF, respectively. It can also be noted that the maxima of the CF time serie are not in phase with the warm ENSO phases and are delayed by approximately 2 months. The CTH and CF anomaly time series have been partitioned for high clouds (defined as clouds with altitude $h > 7$ km), middle clouds (3 km $< h < 7$ km) and low clouds ($h < 3$ km), smoothed with a 6-month running mean and plotted in Fig. 8. The correlation coefficients (calculated with

unsmoothed data) reported on the right clearly indicate that a warm (cold) ENSO phase corresponds to a decrease (increase) in CF for low (R = −0.55) and mid (R = −0.31) clouds, while high clouds increase (decrease) their coverage (R = +0.53). In Fig. 8 it is also shown that the lagged extrema in column-averaged CF of Fig. 7 originate in the lowest layers of the troposphere, because CF for low- and mid-level clouds always anticipate the extrema for high clouds by a constant lag of 2 months.

More precisely, the coupling of CTH and CF to El Niño can be understood inspecting Fig. 9, where R for either cloud parameters has been plotted as function of altitude bin h. Starting from the Planet Boundary Layer (PBL) ($h < 2$ km), a warmer ocean surface produces evaporation and CF increases (R = +0.39), while CTH does not exhibit almost any correlation (R = −0.11). Departing from the PBL (2 km $\leq h < 8$ km), the cloud field is compressed by winds (CF decreases in response to warming, $−0.30 \leq$ R $\leq −0.41$) and convection lifts clouds higher up (CTH increases in response to warming, $+0.16 \leq$ R $\leq +0.38$). Within the upper layer of the troposphere ($h \geq 8$ km), clouds rise until the tropopause ($h \approx 16$–17 km) stops their ascent ($−0.11 \leq$ R ≤ 0) and, concurrently, extend (CF increases, $+0.19 \leq$ R $\leq +0.44$), following the divergent air flow toward zones of lower pressure. This is consistent with the picture of a reinforced meridional circulation which squeezes clouds at low altitudes, while high clouds spread out in the horizontal direction and air masses close the Hadley cell. In fact, positive correlations between CF, SST and surface convergence are found by Norris (2005) for the International Satellite Cloud Climatology Project (ISCCP) high cloud amount and the ground-based Extended Edited Cloud Report Archive (EECRA) high-cloud record, calculated over almost the same region. Conversely, the warm pool situated in the western tropical Pacific (30° N-30° S and 100° E-160°E) is characterized by the reversed situation: deep convective clouds occur during cold La Niña periods. Hence negative correlations between CF and SST are found (Norris, 2005; Marchand, 2013). This dipole-like ENSO influence on cloud properties can be seen in Fig. 10, where diagrams of COT-CTH are drawn for the strongest ENSO within the GSG record (i.e. El Niño April 1997 - May 1998 and the ensuing La Niña June 1998 - June 2001) over the Niño 3.4 index box and the tropical warm pool.

Bjerknes (1969) already pointed out how trade winds and sea surface temperature (SST) mutually strengthen for both ENSO phases. Interestingly, he also argued that the ocean response to a change of the wind circulation patterns during El Niño has a characteristic lag of 2 months (this mechanism is known as *Bjerknes feedback*), such as the lag seen in the CF anomaly time series of Fig. 7 and Fig. 8. It is suggestive to regard this similarity as the manifestation of a two-way coupling between cloud properties and sea surface temperature. However, the dynamical interpretation rather than the energetic interpretation is here preferred for two reasons: not only the curves and the correlations of Fig. 8 have been calculated for the narrow Niño 3.4 climate index box, located in the Central East Pacific, where the effect of the weakening of the longitudinal Walker circulation (corresponding to the onset of teleconnections) is at its maximum, but also Dessler (2011) showed that cloud changes have a negligible impact on SST, due to heat storage capacity and heat transport of the ocean, which

dominates the ENSO climate variability.

The relationship between CTH, CF and ENSO has been investigated by Erlykin and Wolfendale (2010). Through the analysis of the ISCCP cloud cover and top pressure, they assert that both ENSO phases and global Earth's low troposphere temperature are negatively correlated with low-cloud amount. Thus, in the periods influenced by warm El Niño, low clouds are lift higher up and are reclassified as mid-level clouds. The opposite holds true for periods driven by La Niña. Since the last decade is showing more frequently cold episodes (59% versus 41% occurrence of warm phases, see also Loeb et al. (2012)), it is reasonable to suppose that the ENSO pulls clouds down.

4.2 Trends in cloud top height

Fig. 11 supports the argument introduced in the previous section: the removal of ENSO (excluding any data within longitudes of $170°$ W and $120°$ W and latitudes of $5°$ N and $5°$ S) shifts the overall trend, calculated in the latitudinal belt $\pm 60°$ (in order to lessen the influence of ice-capped regions), from -30.26 m to -8.33 m over 17 years.

The time series has been broken up for underlying surface and a trend of -2.51 m yr^{-1} over ocean and $+0.27$ m yr^{-1} over land are identified (lower plot of Fig. 11). No exhaustive explanation can be found for this divergent land/water trend on a global scale, due to the complexity and variety of tropospheric processes influencing the clouds. On a global scale, such effects might average out and give rise to well-defined cloud changes. Even so, it was noted (Wagner et al., 2008) that CTH reacts in response to a change in near-surface temperature (ST). The authors analyzed 7.5 years of GOME data and showed not only a strong positive correlation between CTH and ST, but also that ST changes are highest over land. Thus, at the simplest level, global patterns of ST might explain the informations concealed in the diverging land/ocean CTH trends.

The findings are summarised in Table 3 together with previous results from independent datasets. The reported values show discrepancies. Indeed, the length of datasets as well as the instrumental spatial resolution can alter the rate of linear change in CTH, because different cloud features are sensed, both in space and time. It must be also noted that retrieved cloud properties and, therefore, trends are affected by the choice of the spectral window used in the algorithms. IR-based algorithms are sensitive to cirrus clouds, whereas NIR-based algorithms, such as SACURA, are valid for thick clouds. Moreover, SACURA takes into account O_2 absorption inside the clouds and the retrieved cloud height cannot be regarded as *effective*, since it will be closer to its geometrical top in the case of a single-layer cloud.

Fig. 12 shows global maps of trend magnitude β and standard deviation σ_β, degraded to $5°$-sided cell mesh for computational efficiency and smoothed with the 8 neighboring cells. The maps indicate that trend magnitudes are zonally partitioned. The strongest trends are found over North Africa and the Arabian subcontinent ($> +45$ m yr^{-1}), Central Eastern Pacific (-30 m yr^{-1}) and Indian Ocean (-15 m yr^{-1}). Conversely, the mid-latitudes ($60°$N-$30°$N and $30°$S-$60°$S) are homogeneously char-

305 acterised by a slightly decreasing trend (-2 m yr^{-1} on average). Fig. 12 shows also that the trend variability follows the oceanic contours, being over water almost always greater than 20 m yr^{-1} in the latitude belt $\pm 30°$ and smaller than 15 m yr^{-1} otherwise. Table 4 summarizes zonal values of CTH trend for the tropics and the mid-latitudes, over land and water masses.

Analogous conclusions are indirectly drawn by Marchand (2013), who analysed MISR (on board

310 the TERRA platform) cloud amount as function of cloud (top) height. Specifically, linear trends of cloud amount over oceanic regions are shown in Marchand (2013, Fig. 6, p. 1946). It can be seen that where high cloud amount decreases low clouds are more frequent. This effect can be seen over the North-East Pacific and over the Central East Pacific. Hence the author suggests a net decrease in mean cloud top height. Notwithstanding the different length of the time series (MISR covering the

315 period 2001 to 2011), we observe a similar tendency in CTH over the same regions, which is evident in the left plot of Fig. 12. The opposite also holds true: regions showing increasing occurrence of high clouds exhibit a decrease in low cloud amount. Consequently, the mean cloud top height is expected to increase, as seen over Indonesia and, to a lesser extent, over the Central Atlantic.

Statistically significant (at 95% confidence level) trends are plotted in Fig. 13. No patterns are

320 discernible that can be easily classifiable in the context of natural synoptic cloud variability, except for the decrease over Central East Pacific and the increase over North Africa. The main difference between Fig. 12 and Fig. 13 is that the CTH increase over the Arabian peninsula is not significant. To investigate this effect, the two regions are magnified on a continental scale, labeled R1 (North Africa) and R2 (Arabian Peninsula), and their trends in CTH are plotted in Fig. 14 (top row). Both

325 regions are naturally arid areas, which do not exhibit any notable evaporation. Any cloud field over R1 and R2 is likely the result of moist air transport from neighboring water basins. For this reason, a water vapor (H_2O) dataset has been added and analysed in Fig. 14. The dataset has been derived from the same instruments used for generation of the cloud data records and is described by Noël et al. (2004, 2005) and Mieruch et al. (2008).

330 It can be seen that the significant CTH trend over R1 is sustained by an increasing trend in H_2O. Conversely, the decreasing trend in H_2O over R2, which has been reported to be statistically significant (Mieruch et al., 2008), is anticorrelated with CTH. An explanation may be found in large-scale outflows of fine-mode soot particles, that are produced in the Indian subcontinent during biomass burning seasons and transported over R2 (but not over R1) by easterly winds during the winter phase

335 of the Indian monsoon. Indeed, most of the decreasing trend in H_2O is seen during winter seasons (Fig. 14, mid right), while almost no trend is seen in summer months (Fig. 14, mid left). The absorption of solar radiation by soot gives rise to two competing effects. On one hand, soot warms the atmospheric column (Feingold, 2005) and may cause clouds to dry out (Ackerman et al., 2000). On the other hand, soot depletes the amount of radiation reaching the surface, exerting a negative

340 radiative forcing (Nakajima and Schulz, 2009), and the amount of energy at disposal for evaporation is diminished. Further arguments supporting a decrease in surface insulation of the Indian Ocean

have been reviewed, among others, by Turner and Annamalai (2012).

In general, changes in column-averaged cloud top height might be explained by changes in cloud cover in different altitude layers. When looking at the trend in annual cloud fraction anomalies (not shown here) a constant decreasing tendency is suggested. This is consistent with long-term changes derived by other instruments (Stubenrauch et al., 2013) for the same region. In the bottom row of Fig. 14 the breakups in summer (JJA) and winter (DJF) months are portrayed. Cloud fraction trends don't exhibit seasonality and are not correlated with the seasonal Indian monsoon because the trends over R1 and R2 are commensurate and have equal sign, which wouldn't be otherwise. This finding also complies with Norris (2001).

Moreover, the question whether a change in cloud parameters (fraction, optical thickness and top height) translates into a change in columnar water vapor (due to the assumption in the algorithm of ghost column under the cloud) has been recently addressed by du Piesanie et al. (2013). They analysed SCIAMACHY water vapor columns and cloud products, generated with the same algorithms of the datasets used in this work (AMC-DOAS, Noël et al. (2004, 2005); SACURA, Rozanov and Kokhanovsky (2004)). The authors showed that water vapor columns are influenced neither by changes in cloud fraction nor in cloud optical thickness. The dependence of H_2O total column on changes in cloud top height has been explored for cases with CF $\geqslant$ 0.9. Even for these very cloudy scenes, a change in CTH of ≈ 450 m over 17 years can't explain the decrease of ≈ -0.85 g/cm^{-2} above the Arabian Peninsula for the same time span. This argument rules out algorithmic artifacts due to the shielding of water vapor by clouds and points to a real process, that presumably takes place over the northern Indian Ocean.

5 Conclusions

For the first time, spaceborne passive measurements of the O_2 A-band have been used to identify the rate of linear change (trend) in cloud top height anomalies for the period June 1996–May 2012. The instruments used in this work are hyperspectrally resolved spectrometers (i.e. GOME, SCIAMACHY and GOME-2), payloads of polar orbiting platforms which cross the Equator at mid morning (local time). In particular, it has been seen that the instrumental spatial resolution impacts the calculation of mean values of apparent cloud top height at a monthly sampling. Owing to the sensing time lag among the instruments, the anomaly time series have been calculated for each sensor separately, once the climatological mean state of the cloud property of interest has been subtracted. Given that cloud top height, at monthly sampling, does not exhibit any significant persistence in time, the rate of linear change has been calculated with linear regression methods. The estimation of the distribution of cloud top height trends with bootstrap technique enabled the computation of confidence intervals and, consequently, the assessment of statistical significance.

First, cloud top height and, to a minor extent, cloud cover have been found to be coupled to ENSO

11

in a dipole-like fashion across the Pacific Ocean. Patterns of cloud top height autocorrelation of magnitude $0.12-0.13$ (vanishing after approximately 6 months) are seen over the Central East Pacific, Atlantic and Indian Oceans, resembling the large scale fluctuations induced by ENSO. Moreover, the hallmark of the cold tongue in the central eastern Pacific is correlated with the strongest decreasing trend in cloud top height. The anomaly time serie of Fig. 3 clearly exhibits two dips, centered at the beginning of year 2000 and 2011. They resemble La Niña's periodicity, pointing to the ENSO's role played in the overall decreasing trend in cloud top height.

Second, except for trends derived from the same instrument (i.e. GOME), the comparison with trends previously published in the literature displays differences, which cannot be easily understood within a single explanation. In the case of MODIS and MISR trends (Evan and Norris, 2012), one notes that those instruments not only differ in spatial sampling but also are sensitive to thin clouds, in both solid and liquid phase. These clouds cannot be detected with the hyperspectral sensors in the O_2 A-band used in this work. Thus, the biases shown in Table 3 might point to a recent increasing trend of thin, typically cirrus, clouds. This argument could be also substantiated by the moderate decreasing CTH trend seen in both hemispherical mid-latitudes: since there is evidence on the widening of the Hadley cell (Allen et al., 2012, and references therein), the poleward displacement of cloudiness (Eastman and Warren, 2013) and the concurrent upward shift of high clouds on a synoptic scale (inferred from modeling studies, Singh and O'Gorman (2012)), this picture would imply a systematic thermodynamic phase change in high clouds. As a consequence, a lower occurrence of warm (liquid) clouds in the upper atmospheric layers suggests a higher occurrence of cirrus clouds (undetectable with the O_2 A-band), with the net effect of lowering the mean columnar cloud top height, as seen in the current dataset.

Preliminary analysis of the trends seen over North Africa and Arabian Peninsula suggests a semi-direct aerosol effect on clouds. Natural and anthropogenic soot particles have an impact on cloud top height, modulating insulation and water evaporation over the Indian Ocean. Subsequently, during the winter phase of the Indian Monsoon, transport of moist air masses over the arid Arabian Peninsula exerts a negative feedback and decreases statistical significance of clouds' vertical displacement. In fact, this effect has been already seen over Europe during the economic, industrial and infrastructural adjustments following the fall of the East Bloc (Devasthale et al., 2005). However, this topic deserves in-depth investigation, which we defer to a later publication.

In general, the representativeness of every trend is affected by the record length under study. 17 years of data still might not be enough to provide any decisive answer to current open questions involving clouds. Therefore, future planned Earth's observing missions, such as Metop-C and Sentinel-5 precursor with their respective payloads GOME-2 and TROPOMI (Veefkind et al., 2012), will enable the extension of the existing cloud records until and beyond 2022, supporting attribution studies of cloud property changes to natural or human causes and assessments of the cloud feedback sign within the climate system.

Appendix A

Algorithm sensitivity to calibration drift

In this appendix we assess the sensitivity of the SACURA algorithm to three distinct calibration errors. The question to be answered is whether the shifts in the time series of absolute values of CTH (see Fig. 1) can be caused by calibration differences among the three sensors used in this work.

To this purpose, an input radiance in the O_2 A-band (in range 758–772 nm) is simulated, neglect-
420   ing polarization, with the radiative transfer model SCIATRAN (Rozanov et al., 2014). It corresponds to a single-layer cloud, placed at 5 km (top) and 4 km (bottom altitude) and optically thick 20. COT is set equal to 20 because its global distribution peaks about this value (Lelli et al., 2012). The solar zenith angle is set equal to 60° with a dark underlying surface. From top to bottom of Fig. 15, the relative error (%) in COT, the absolute error (km) in CTH and CBH are plotted, respectively. For
425   the black curves, the radiance is perturbed only at λ=758 nm. For the red curves, a constant offset has been added in range 758–772 nm, meaning a shift of the oxygen A-band. For the blue curves, a wavelength-dependent offset has been added to the whole band. The spectral behavior of the calibration error has been taken from Noël (2005) and is considered linear from λ=758 nm ($\pm$ 0.86%) throughout λ=772 nm ($\pm$ 0.80%). Clearly, this last error parameterization is also the most realistic
430   as compared to the single-channel perturbation in the continuum outside the band.

From the analysis of Fig. 15, the following conclusions, relevant to the scope of this paper, can be drawn: first, spectral-dependent calibration errors have almost no impact on the retrieved cloud top height. The CTH bias (mid plot, blue curve) is stable about a value of ≈ 250 m, which is the error introduced by the analytical forward model (Lelli et al., 2012, Fig. 1, p. 1556). Second, in
435   case of calibration errors, cloud bottom height is the affected parameter. The bottom plot clearly shows that CBH becomes noisier. It can also be seen that errors in retrieved cloud optical thickness (top plot) don't influence the retrieved CTH and that are independent on the applied error, because COT is retrieved at the single channel λ=758 nm, while CTH and CBH are retrieved across the whole A-band, after normalization to the average value of reflectance outside the band. Therefore,
440   we conclude that the primary role in the shifts among time series of absolute CTH values (Fig. 1) is played by the different spatial resolution among the instruments and not by radiometric calibration.

450

References

Ackerman, A. S., Toon, O. B., Stevens, D. E., Heymsfield, A. J., Ramanathan, V., and Welton, E. J.: Reduction of Tropical Cloudiness by Soot, Science, 288, 1042–1047, doi:10.1126/science.288.5468.1042, 2000.

Allen, R. J., Sherwood, S. C., Norris, J. R., and Zender, C. S.: Recent Northern Hemisphere tropical expansion primarily driven by black carbon and tropospheric ozone, Nature, 485, 350–354, doi:10.1038/nature11097, 2012.

Bjerknes, J.: Atmospheric teleconnections from the Equatorial Pacific, Monthly Weather Review, 97, 163–172, doi:10.1175/1520-0493(1969)097<0163:ATFTEP>2.3.CO;2, 1969.

Bovensmann, H., Burrows, J. P., Buchwitz, M., Frerick, J., Noël, S., Rozanov, V. V., Chance, K. V., and Goede, A. P. H.: SCIAMACHY: Mission objectives and measurement modes, J. Atmos. Sci., 56, 127–150, doi:doi: 10.1175/1520-0469(1999)056<0127:SMOAMM>2.0.CO;2, 1999.

Burrows, J. P., Weber, M., Buchwitz, M., Rozanov, V. V., Ladstätter Weissenmayer, A., Richter, A., DeBeek, R., Hoogen, R., Bramstedt, K., Eichmann, K. U., Eisinger, M., and Perner, D.: The Global Ozone Monitoring Experiment (GOME): Mission Concept and First Scientific Results, J. Atmos. Sci., 56, 151–175, doi:10.1175/1520-0469, 1999.

Callies, J., Corpaccioli, E., Eisinger, M., Hahne, A., and Lefebvre, A.: GOME-2- Metop's second-generation sensor for operational ozone monitoring, ESA bulletin, 102, 28–36, 2000.

Clement, A. C., Burgman, R., and Norris, J. R.: Observational and Model Evidence for Positive Low-Level Cloud Feedback, Science, 325, 460–464, doi:10.1126/science.1171255, 2009.

Davies, R. and Molloy, M.: Global cloud height fluctuations measured by MISR on Terra from 2000 to 2010, Geophys. Res. Lett., 39, L03 701, doi:10.1029/2011GL050506, 2012.

Dessler, A. E.: Cloud variations and the Earth's energy budget, Geophys. Res. Lett., 38, L19 701, doi:10.1029/2011GL049236, 2011.

Devasthale, A., Kruger, O., and Graßl, H.: Change in Cloud-Top Temperatures Over Europe, IEEE Geo. Rem. Sens. Lett., 2, 333–336, 2005.

du Piesanie, A., Piters, A. J. M., Aben, I., Schrijver, H., Wang, P., and Noël, S.: Validation of two independent retrievals of SCIAMACHY water vapour columns using radiosonde data, Atmos. Meas. Tech., 6, 2925–2940, doi:10.5194/amt-6-2925-2013, 2013.

Eastman, R. and Warren, S. G.: A 39-Yr Survey of Cloud Changes from Land Stations Worldwide 1971–2009: Long-Term Trends, Relation to Aerosols, and Expansion of the Tropical Belt, J. Clim., 26, 1286–1303, doi:10.1175/JCLI-D-12-00280.1, 2013.

Efron, B. and Tibshirani, R. J.: An Introduction to the Bootstrap, Chapman & Hall, New York, 1993.

Erlykin, A. D. and Wolfendale, A. W.: Global Cloud Cover and the Earth's Mean Surface Temperature, Surveys in Geophysics, 31, 399–408, doi:10.1007/s10712-010-9098-7, 2010.

EUMETSAT: GOME-2 PMD Band Definitions 3.0 and PMD Calibration, Tech. Rep. EUM/OPS-EPS/DOC/07/0601, EUMETSAT, Darmstadt, Germany, 2010.

Evan, A. T. and Norris, J. R.: On global changes in effective cloud height, Geophys. Res. Lett., 39, L19 710, doi:10.1029/2012GL053171, 2012.

Feingold, G.: On smoke suppression of clouds in Amazonia, Geophys. Res. Lett., 32, L02 804, doi:10.1029/2004GL021369, 2005.

Koelemeijer, R. B. A., Stammes, P., Hovenier, J. W., and de Haan, J. F.: A fast method for retrieval of cloud
parameters using oxygen A band measurements from the Global Ozone Monitoring Experiment, J. Geophys.
Res., 106, 3475–3490, doi:10.1029/2000JD900657, 2001.

Koelemeijer, R. B. A., de Haan, J. F., and Stammes, P.: A database of spectral surface reflectivity
in the range 335-772 nm derived from 5.5 years of 0.5 observations, J. Geophys. Res., 108, 4070,
doi:10.1029/2002JD002429, http://www.temis.nl/data/ler.html, 2003.

Kokhanovsky, A. A. and Rozanov, V. V.: The physical parameterization of the top-of-atmosphere reflection
function for a cloudy atmosphere–underlying surface system: the oxygen A-band case study, J. Quant. Spec-
trosc. Rad., 85, 35–55, doi:10.1016/S0022-4073(03)00193-6, 2004.

Kokhanovsky, A. A., Mayer, B., Rozanov, V. V., Wapler, K., Burrows, J. P., and Schumann, U.: The influence
of broken cloudiness on cloud top height retrievals using nadir observations of backscattered solar radiation
in the oxygen A-band, J. Quant. Spectrosc. Rad., 103, 460 – 477, doi:10.1016/j.jqsrt.2006.06.003, 2007.

Laken, B., Palle, E., and Miyahara, H.: A Decade of the Moderate Resolution Imaging Spectroradiometer: Is a
Solar–Cloud Link Detectable?, J. Clim., 25, 4430–4440, doi:10.1175/JCLI-D-11-00306.1, 2012.

Lelli, L., Kokhanovsky, A. A., Rozanov, V. V., Vountas, M., Sayer, A. M., and Burrows, J. P.: Seven years of
global retrieval of cloud properties using space-borne data of GOME, Atmos. Meas. Tech., 5, 1551–1570,
doi:10.5194/amt-5-1551-2012, 2012.

Loeb, N. G., Kato, S., Su, W., Wong, T., Rose, F. G., Doelling, D. R., Norris, J. R., and Huang, X.: Ad-
vances in Understanding Top-of-Atmosphere Radiation Variability from Satellite Observations, Surveys in
Geophysics, 33, 359–385, doi:10.1007/s10712-012-9175-1, 2012.

Loyola, D. G. and Ruppert, T.: A new PMD cloud-recognition algorithm for GOME, ESA Earth Observation
Quarterly, 58, 45–47, 1998.

Loyola, D. G., Thomas, W., Spurr, R., and Mayer, B.: Global patterns in daytime cloud proper-
ties derived from GOME backscatter UV-VIS measurements, Int. J. Remote Sens., 31, 4295–4318,
doi:10.1080/01431160903246741, 2010.

Marchand, R.: Trends in ISCCP, MISR, and MODIS cloud-top-height and optical-depth histograms, J. Geo-
phys. Res. Atmos., 118, 1941–1949, doi:10.1002/jgrd.50207, 2013.

Marshak, A., Davis, A., Wiscombe, W., and Titov, G.: The verisimilitude of the independent pixel approxi-
mation used in cloud remote sensing, Rem. Sens. Environ., 52, 72–78, doi:10.1016/0034-4257(95)00016-T,
1995.

Mieruch, S., Noël, S., Bovensmann, H., and Burrows, J. P.: Analysis of global water vapour trends from satellite
measurements in the visible spectral range, Atmos. Chem. Phys., 8, 491–504, doi:10.5194/acp-8-491-2008,
2008.

Mudelsee, M.: Climate Time Series Analysis: Classical Statistical and Bootstrap Methods, Atmospheric
and Oceanographic Sciences Library, Vol. 42, Springer, Dordrecht Heidelberg London New York,
doi:10.1007/978-90-481-9482-7, 2010.

Nakajima, T. and Schulz, M.: What Do We Know about Large-scale Changes of Aerosols, Clouds, and the
Radiation Budget?, in: Clouds in the Perturbed Climate System, edited by Heintzenberg, J. and Charlson,
R. J., Strüngmann Forum Reports, pp. 401–432, MIT Press, Cambridge, Massachusetts, 2009.

Noël, S.: Determination of Correction Factors for SCIAMACHY Radiances and Irradiances, Tech. Rep. IFE-

SCIA-SN-20050203 (Issue 5.2), Institute of Environmental Physics and Remote Sensing, University of Bremen, Germany, http://www.iup.uni-bremen.de/sciamachy/SCIA_CAL/irrad_corr.pdf, 2005.

Noël, S., Buchwitz, M., and Burrows, J. P.: First retrieval of global water vapour column amounts from SCIA-MACHY measurements, Atmos. Chem. Phys., 4, 111–125, doi:10.5194/acp-4-111-2004, 2004.

Noël, S., Buchwitz, M., Bovensmann, H., and Burrows, J. P.: Validation of SCIAMACHY AMC-DOAS water vapour columns, Atmos. Chem. Phys., 5, 1835–1841, doi:10.5194/acp-5-1835-2005, 2005.

Norris, J. R.: Has northern Indian Ocean cloud cover changed due to increasing anthropogenic aerosol?, Geophys. Res. Lett., 28, 3271–3274, doi:10.1029/2001GL013547, 2001.

Norris, J. R.: Trends in upper-level cloud cover and surface divergence over the tropical Indo-Pacific Ocean between 1952 and 1997, J. Geophys. Res., 110, D21 110, doi:10.1029/2005JD006183, 2005.

Rozanov, V. V. and Kokhanovsky, A. A.: Semianalytical cloud retrieval algorithm as applied to the cloud top altitude and the cloud geometrical thickness determination from top-of-atmosphere reflectance measurements in the oxygen A band, J. Geophys. Res., 109, 4070, doi:10.1029/2003JD004104, 2004.

Rozanov, V. V., Rozanov, A. V., Kokhanovsky, A. A., and Burrows, J. P.: Radiative transfer through terrestrial atmosphere and ocean: Software package SCIATRAN, J. Quant. Spectrosc. Rad., 133, 13–71, doi:10.1016/j.jqsrt.2013.07.004, 2014.

Schulzweida, U., Müller, R., Kornblüh, L., Ansorge, C., and Quast, R.: CDO - Climate Data Operators - v1.5.9, Center for Marine and Atmospheric Sciences (ZMAW), Max-Planck Institute for Meteorology, University of Hamburg, https://code.zmaw.de/projects/cdo, 2012.

Singh, M. S. and O'Gorman, P. A.: Upward Shift of the Atmospheric General Circulation under Global Warming: Theory and Simulations, J. Clim., 25, 8259–8276, doi:10.1175/JCLI-D-11-00699.1, 2012.

Solomon, A. and Newman, M.: Reconciling disparate twentieth-century Indo-Pacific ocean temperature trends in the instrumental record, Nature Climate Change, 2, 691–699, doi:10.1038/NCLIMATE1591, 2012.

Stubenrauch, C. J., Rossow, W. B., Kinne, S., Ackerman, S., Cesana, G., Chepfer, H. Getzewich, B., Di Girolamo, L., Guignard, A., Heidinger, A., Maddux, B., Menzel, P., Minnis, P., Pearl, C., Platnick, S., Riedi, J., Sun-Mack, S., Walther, A., Winker, D., Zeng, S., and Zhao, G.: Assessment of Global Cloud Datasets from Satellites: Project and Database Initiated by the GEWEX Radiation Panel, Bull. Amer. Meteorol. Soc., pp. 0003–0007, doi:10.1175/BAMS-D-12-00117, 2013.

Trenberth, K. E.: The definition of El Niño, Bull. Amer. Meteorol. Soc., 78, 2771–2777, doi:10.1175/1520-0477(1997)078<2771:TDOENO>2.0.CO;2, 1997.

Turner, A. and Annamalai, H.: Climate change and the South Asian summer monsoon, Nature Climate Change, 2, 587–595, doi:10.1038/nclimate1495, 2012.

U. S. National Centers for Environmental Prediction (NCEP): Oceanic Niño Index (ONI), National Oceanic and Atmospheric Administration (NOAA), http://www.cpc.ncep.noaa.gov/products/precip/CWlink/MJO/enso.shtml, (last access: January 2013), 1993.

van Diedenhoven, B., Hasekamp, O. P., and Aben, I.: Surface pressure retrieval from SCIAMACHY measurements in the O_2 A Band: validation of the measurements and sensitivity on aerosols, Atmos. Chem. Phys., 5, 2109–2120, doi:10.5194/acp-5-2109-2005, 2005.

Veefkind, J. P., Aben, I., McMullan, K., Förster, H., de Vries, J., Otter, G., Claas, J., Eskes, H. J., de Haan, J. F., Kleipool, Q., Van Weele, M., Hasekamp, O., Hoogeveen, R., Landgraf, J., Snel, R., Tol, P., Ingmann, P.,

17

Voors, R., Kruizinga, B., Vink, R., Visser, H., and Levelt, P. F.: TROPOMI on the ESA Sentinel-5 Precursor:

575   A GMES mission for global observations of the atmospheric composition for climate, air quality and ozone
       layer applications, Rem. Sens. Environ., 120, 70–83, doi:10.1016/j.rse.2011.09.027, 2012.

Wagner, T., Beirle, S., Deutschmann, T., Grzegorski, M., and Platt, U.: Dependence of cloud properties derived
       from spectrally resolved visible satellite observations on surface temperature, Atmos. Chem. Phys., 8, 2299–
       2312, doi:10.5194/acp-8-2299-2008, 2008.

580 Wessel, P. and Smith, W. H. F.: New, improved version of Generic Mapping Tools (GMT) released, Eos Trans.
       AGU, 79, 579–579, doi:10.1029/98EO00426, 1998.

Wilks, D. S.: Statistical Methods in the Atmospheric Sciences, Volume 100, Third Edition (International Geo-
       physics), Academic Press, 2011.

Table 1. Technical specifications of the instruments used in this work. The bottom part of the table describes the Polarization Measuring Devices (PMD).

	GOME	SCIAMACHY	GOME-2
Data availability	$1996 - 2011^{a,b}$	$2002 - 2012^c$	$2007 - 2022^d$
Equator crossing (LT)	10:30 AM	10:00 AM	9:30 AM
Global coverage [days]	3	6	1.5
Spectral coverage [nm]	$237 - 794$	$240 - 2400$	$237 - 794$
Spectral resolution [nm]	0.38	0.44	0.48
Viewing geometry	nadir	nadir, limb, occultation	nadir
Ground pixel size [km^2]	320×40	60×40	80×60
Swath width [km]	≈ 960	≈ 1000	≈ 1920
Polarization	3p	6p	12 (s,p)
Spectral resolution [nm]	$100 - 160$	$55 - 120$	$2.8 - 40$
Spatial resolution [km^2]	40×20	30×7.5	40×5

[a]Global coverage lost in May 2003. [b]Payload has been switched-off since July 2011. [c]Lost contact on April 8, 2012. [d]Foreseen extension of GOME-2 records aboard Metop-B/C.

Table 2. Description of the height grid for calculation and anaylsis of cloud top height time series.

Cloud type	Height range [km]	Bins
Low	$0 - 3$	$1 - 1.5$ km, $1.5 - 2$ km, $2 - 2.5$ km, $2.5 - 3$ km
Middle	$3 - 7$	$3 - 5$ km, $5 - 7$ km
High	$7 - 17$	$7 - 9$, $9 - 11$ km, $11 - 13$ km, $13 - 15$ km, $15 - 17$ km

Table 3. Overview of trends in cloud height [m decade^{-1}][a]. Trends derived from the GSG dataset are given with (left column) and without (right column) ENSO, that has been filtered masking any data within the Niño 3.4 climate index box 170° W - 120° W, 5° N - 5° S

Base period [year/month]	MISR	MISR corr.	MODIS	GOME	GSG	
03/03 – 11/02	−40.1[1]	+54.3[2]	+60.9[2]	-	−10.7	+8.4
96/06 – 03/05	-	-	-	-47.9[⋆,3]	−67.2[⋆]	+25.2[⋆]
96/06 – 12/05	-	-	-	-	−17.8	−4.9

[a]The GSG trends are recalculated for the length of the referenced dataset and latitude belt ±60°.

[1]Davies and Molloy (2012). [2]Evan and Norris (2012). [3]Loyola et al. (2010). [⋆]Extrapolated to decade.

Table 4. Overview of zonal trends in cloud top height [m yr^{-1}]. ENSO excluded masking any data within the box 170° W - 120° W, 5° N - 5° S. Bootstrap resamples $n = 10^3$. The zonal values are not weighted by the respective land and water abundances.

	Belt		Land + Water	Land	Water
With ENSO	Tropics	5° N - 5° S	−4.34±5.65	−1.56±4.02	−5.15±8.21
		20° N - 20° S	−2.16±2.97	1.83±4.40	−3.39±5.32
	Mid latitude	30° N - 60° N	−2.17±1.52	−2.85±4.23	−1.52±3.68
		30° S - 60° S	−2.71±2.59	−2.70±9.25	−2.71±2.47
Without ENSO	Tropics	5° N - 5° S	−1.80±6.00	−1.43±5.05	−1.99±8.52
		20° N - 20° S	0.53±3.53	5.93±5.33	−1.74±4.36
	Mid latitude	30° N - 60° N	−2.11±3.09	−2.72±4.60	−1.53±3.70
		30° S - 60° S	−2.78±2.54	−3.24±8.77	−2.75±2.35
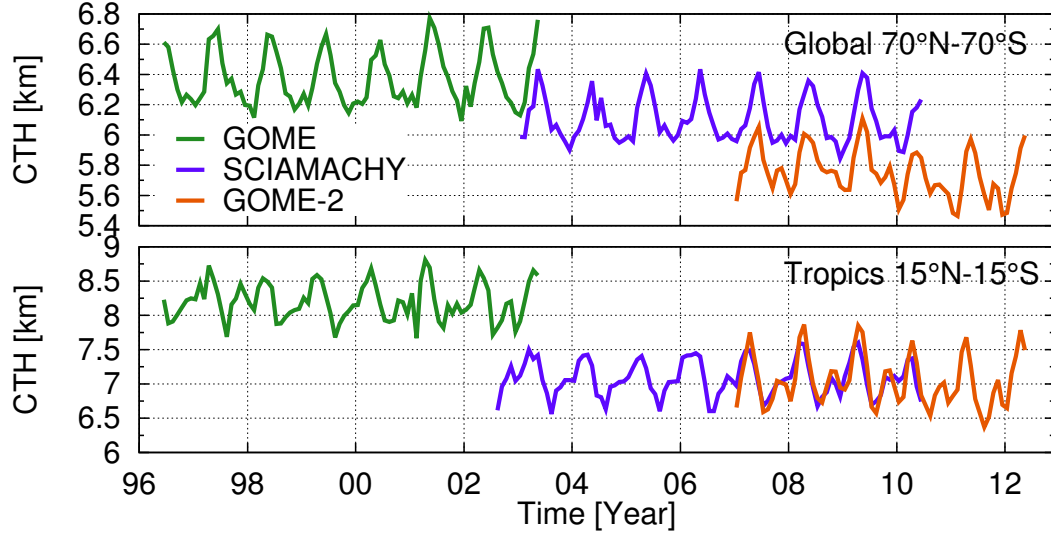
Fig. 1. Time series of monthly means of cloud top height for global (top) and tropical (bottom) region.
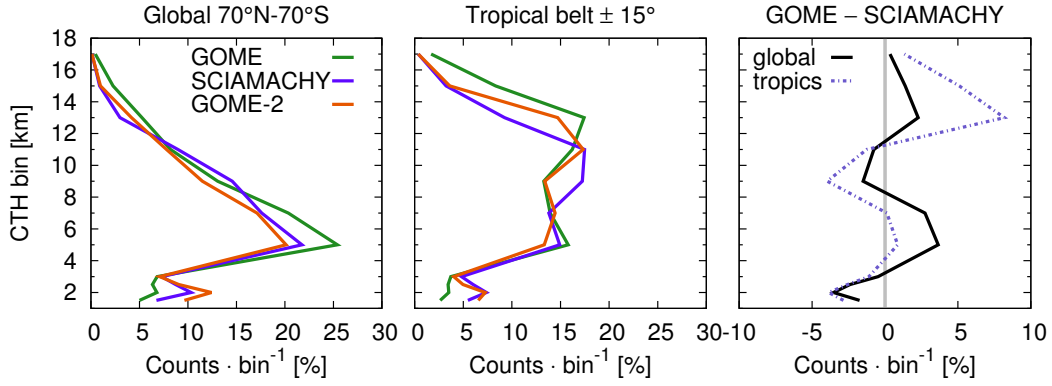
Fig. 2. Relative pixel count as function of height for different instruments for global (left) and tropical (mid) region. (Right) Count difference between GOME and SCIAMACHY. The coarse GOME footprint favors the detection of high clouds over low clouds.
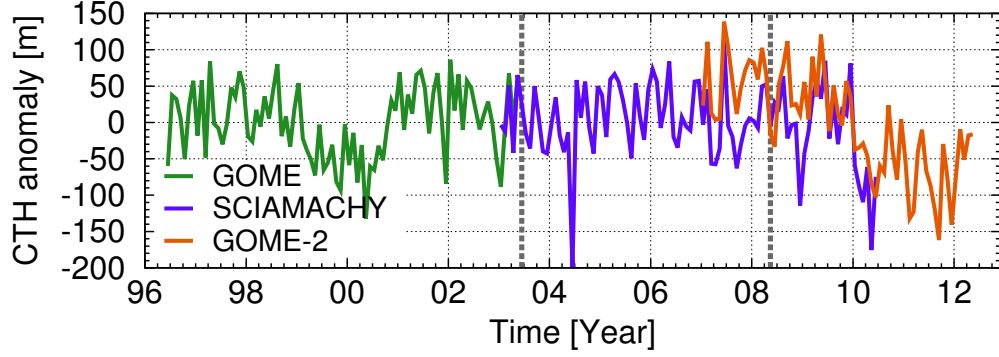
Fig. 3. Monthly means of cloud top height anomaly. The dashed gray vertical lines show the months at which the time series have been merged (June 2003 and May 2008).
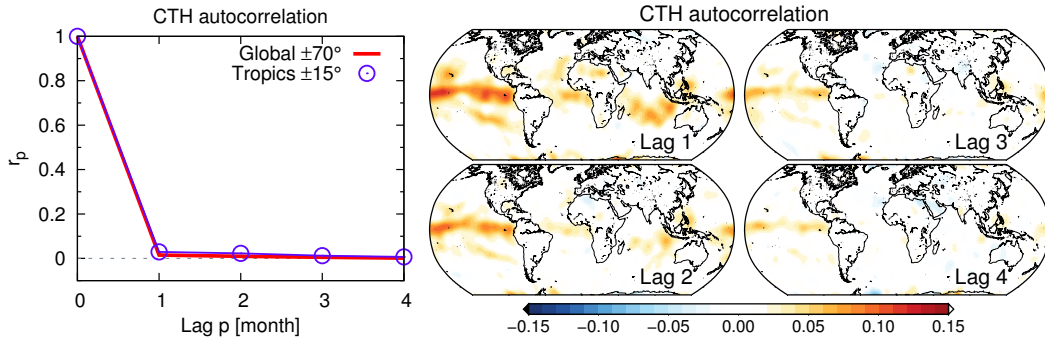
Fig. 4. (Left plot) Autocorrelation function of cloud top height anomalies. Unlagged data ($p = 0$) correlate perfectly with themselves ($r_0 = 1$). r_p decays to almost 0 already at $p = 1$. (Right plot) Maps of CTH autocorrelation for the first 4 months. ENSO-related patterns are seen over Pacific, Indian and Atlantic Oceans.
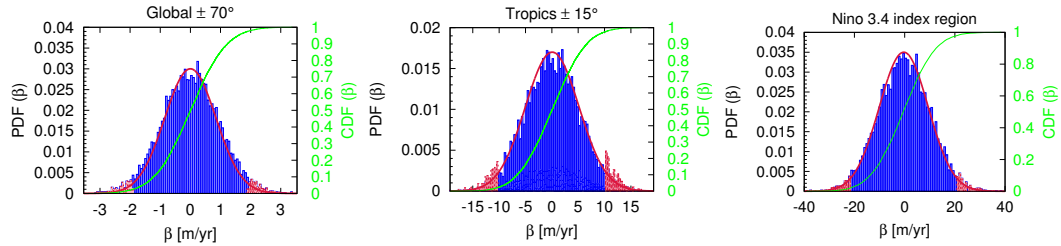
Fig. 5. Normalised bootstrap (resamples $n = 10^4$) distributions of trend β for global (left), tropical (mid) regions and Central East Pacific ($170°$ W-$120°$ W, $5°$ N-$5°$ S). The red tails indicate the confidence interval (CI) at 95%. A Gaussian distribution and a cumulative distribution function are plotted in red and green, respectively.
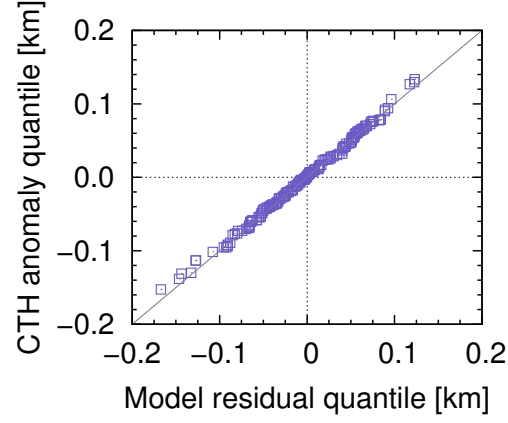
Fig. 6. Normal quantile-quantile plot for global cloud top height anomalies versus the theoretical residual quantiles estimated after regression with Eq. 3 and application of the parameter estimates $\hat{\alpha}$ and $\hat{\beta}$.
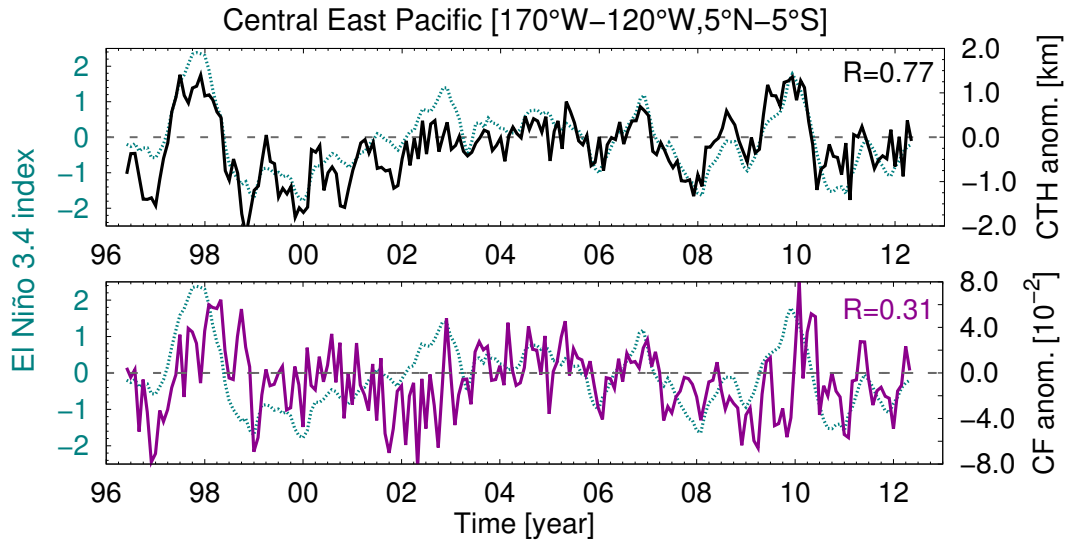
Fig. 7. Time series of cloud top height (top) and cloud fraction (bottom) anomaly over the Central East Pacific with the El Niño 3.4 index.
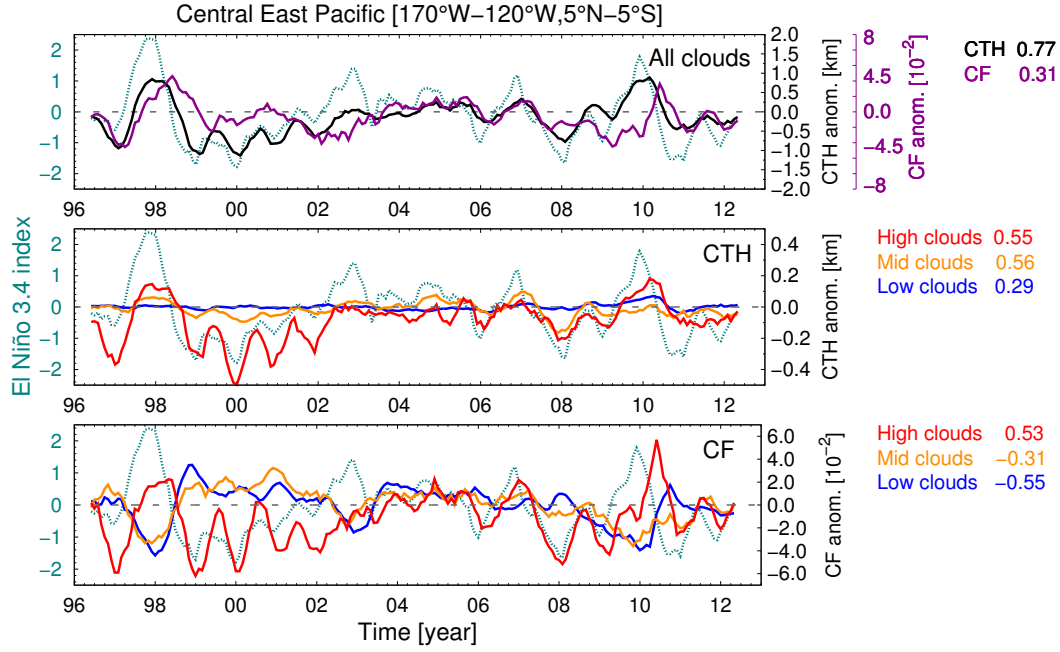
Fig. 8. (Top plot) Time series of cloud top height (black curve) and cloud fraction (purple) anomaly over the Central East Pacific with the El Niño 3.4 index and Pearson's correlation coefficient. (Mid plot) CTH and (bottom plot) CF anomalies subset for low- (blue), mid- (orange), and high-level (red) clouds. Time series smoothed with a 6-month running mean. Correlation coefficients calculated with unsmoothed data.
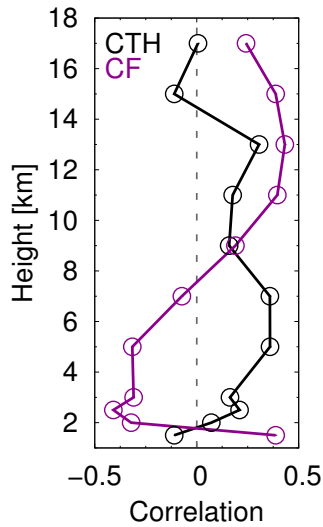
Fig. 9. Correlation coefficient of CTH and CF with the El Niño 3.4 index as function of height for the 17 years of the GSG dataset. Region considered: Central East Pacific (170° W-120° W, 5° N-5° S).
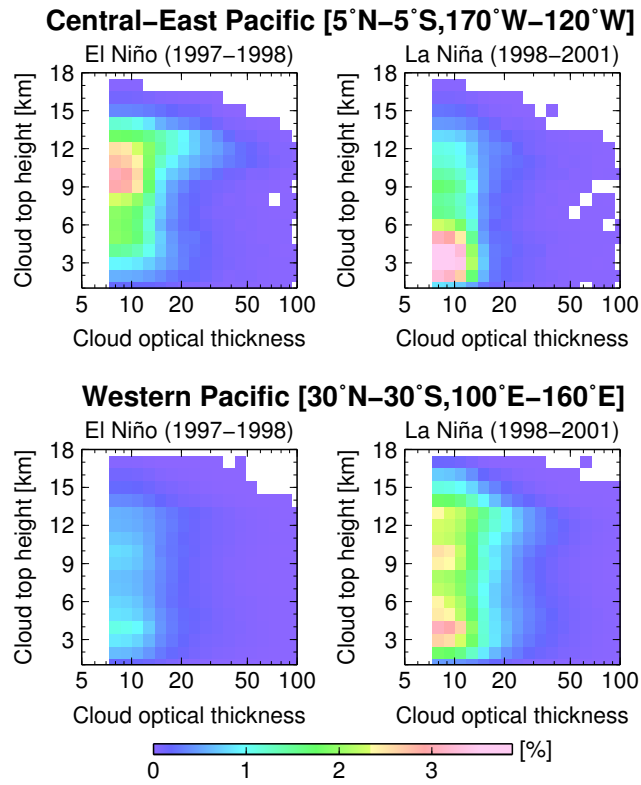
Fig. 10. ISCCP-like diagrams of cloud optical thickness vs. cloud top height for a warm (left column) and cold (right column) ENSO phase between April 1997 and June 2011 over the Niño 3.4 index box (top row) and the western tropical warm pool (bottom row).
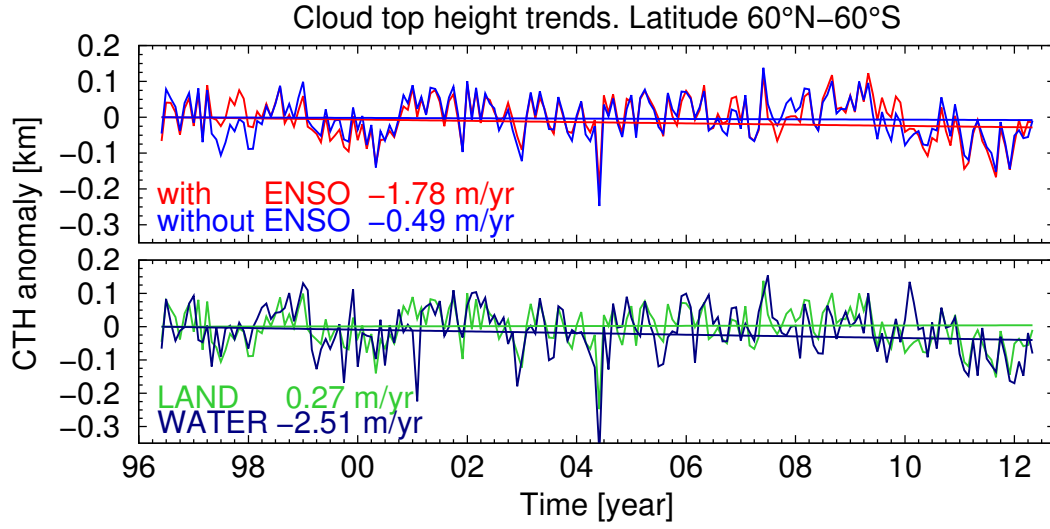
Fig. 11. (Upper plot) Global trend β in CTH anomalies in the latitude belt $\pm 60°$, with (red line) and without (blue line) ENSO region. (Lower plot) The time series are broken up for underlying surface. Abundances of land and water masses between $60°$N and $60°$S are 0.264 and 0.736, respectively.
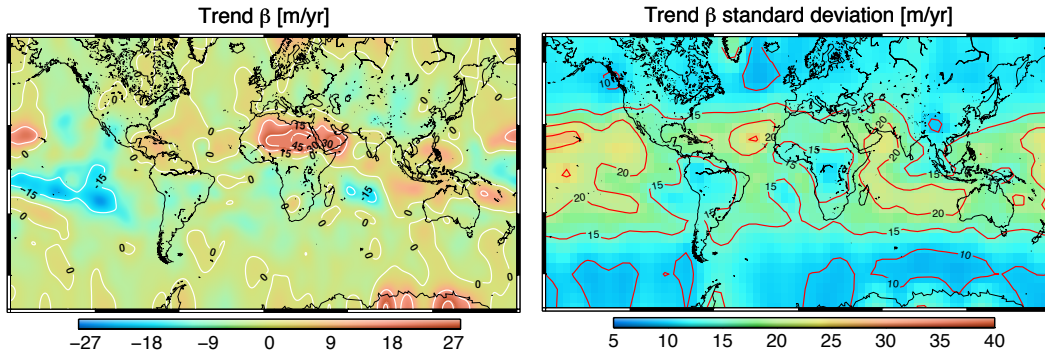

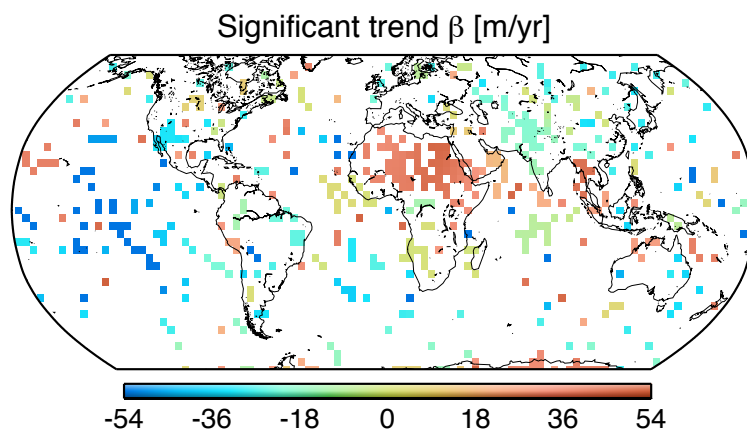**Fig. 12.** Global map of linear trend β in CTH (left) and standard deviation σ_β (right).

Fig. 13. Global trend β in CTH anomaly, statistically significant at 95% confidence level. Data are gridded onto a mesh of 2°-sided cells.
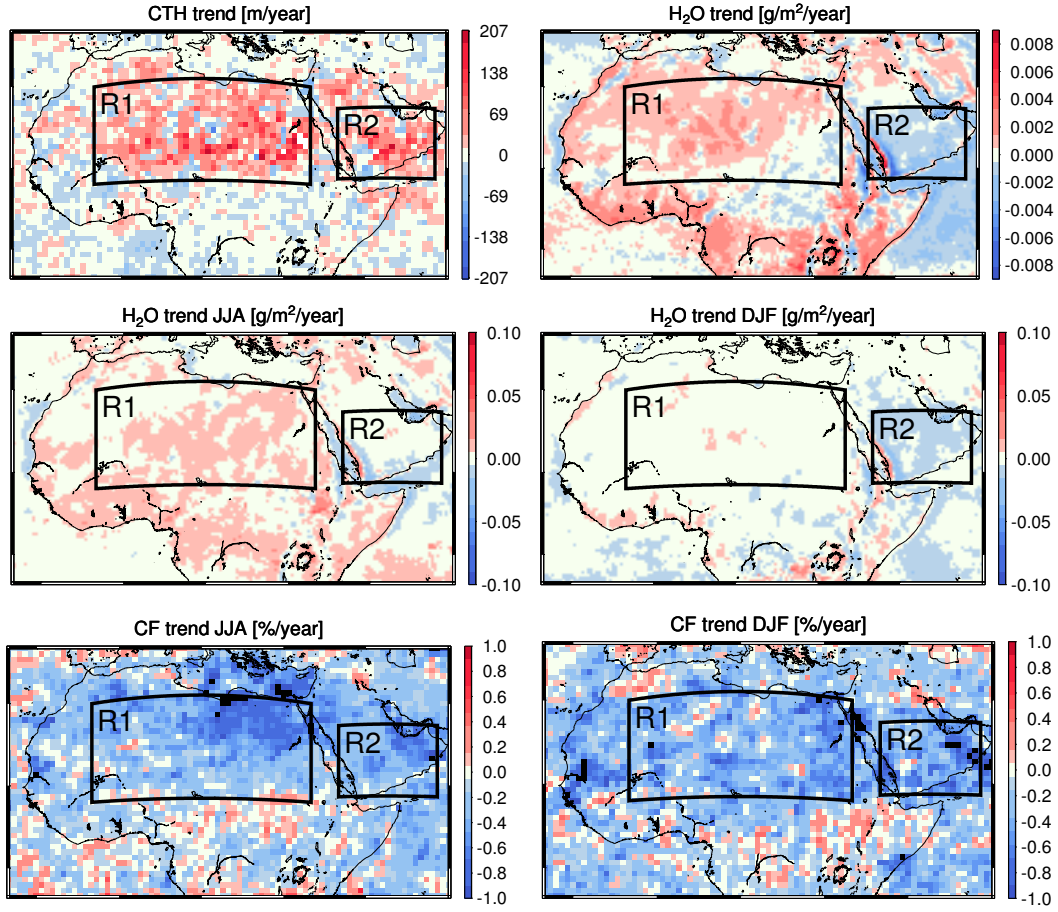
Fig. 14. Maps of linear trends over North Africa (R1) and Arabian Peninsula (R2) for (top left) CTH anomalies and (top right) columnar water vapor anomalies [g/m^2/yr]. The latter is subset for (mid left) summer (JJA) and (mid right) winter (DJF) months. Linear trends for CF anomalies are plotted in the bottom row, for summer (left) and winter (right) months.
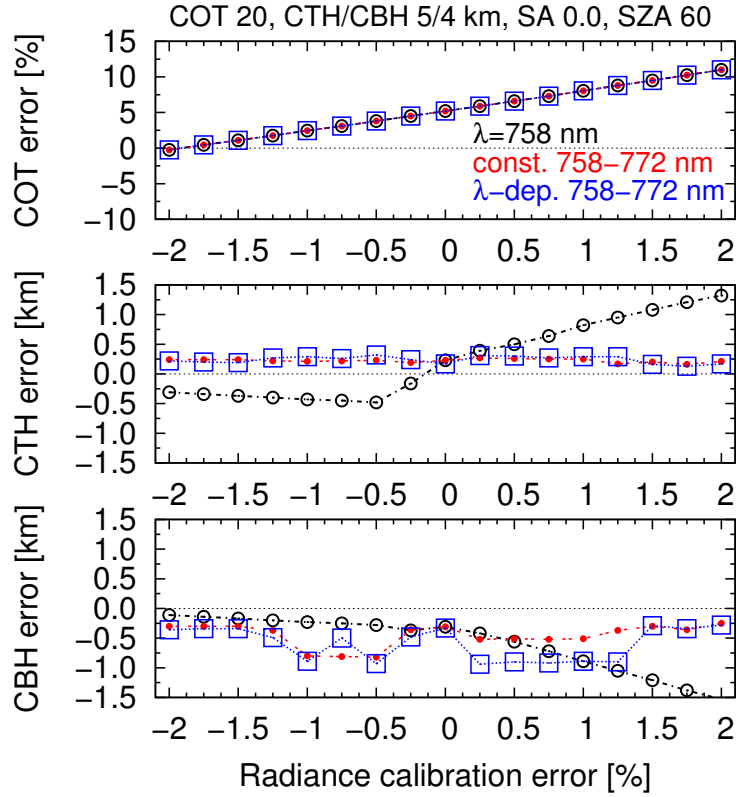
Fig. 15. Errors in retrieved cloud optical thickness (%, top plot), cloud top and bottom height (km, mid and bottom plot) for a single-layered cloud, placed at 5-4 km altitude and optically dense 20, above a dark surface. Three different offsets in radiance are applied: single-channel at λ=758 nm (black curves); constant, added along the whole band (red curves); linearly spectral-dependent, as described in Noël (2005) (blue curve).